Ionic covalent organic nanosheet–polybenzimidazole nanocomposite membranes: modulating membrane capacitive deionization performance via pore architecture

Robert McNair,[1,2‡] Sushil Kumar,[3‡] A.D. Dinga Wonanke,[4] Matthew Addicoat,[4] Robert A.W. Dryfe,[2,5,6] and Gyorgy Szekely[1,3,*]

[1]Department of Chemical Engineering & Analytical Science, University of Manchester, Sackville Street, Manchester M1 3BB, United Kingdom

[2]Department of Chemistry, University of Manchester, Oxford Road, Manchester M13 9PL, United Kingdom

[3]Advanced Membranes and Porous Materials Center, Physical Science and Engineering Division (PSE), King Abdullah University of Science and Technology (KAUST), Thuwal, 23955-6900, Saudi Arabia

[4]School of Science and Technology, Nottingham Trent University, Nottingham, United Kingdom

[5]National Graphene Institute, University of Manchester, Oxford Road, Manchester M13 9PL, United Kingdom

[6]Henry Royce Institute for Advanced Materials, University of Manchester, Oxford Road, Manchester M13 9PL, United Kingdom

[*]Corresponding author: gyorgy.szekely@kaust.edu.sa, www.szekelygroup.com, +966128082769

[‡]These authors equally contributed.

Abbreviations: MCDI – membrane capacitive deionization, iCON – ionic covalent organic nanosheet, QPBI – quaternized polybenzimidazole, RO – reverse osmosis, ED – electrodialysis, MSF – multistage flash distillation, IEM – ion-exchange membrane, AEM – anion-exchange membrane, CEM – cation-exchange membrane, IEC – ion-exchange capacity, SAC – Salt-adsorption capacity, ASAR – average salt-adsorption rate, ENAS – energy normalized to adsorbed salt

ABSTRACT:

Membrane capacitive deionization (MCDI) is a promising technique to achieve desalination of low-salinity water resources. The primary requirements for developing and designing materials for MCDI applications are large surface area, high wettability to water, high conductivity, and efficient ion-transport pathways. Herein, we synthesized ionic covalent organic nanosheets (iCONs) containing guanidinium units that carry a positive charge. A series of quaternized polybenzimidazole (QPBI)/iCON (iCON@QPBI) nanocomposite membranes was fabricated using solution casting. The surface, thermal, wettability, and electrochemical properties of the iCON@QPBI nanocomposite membranes were evaluated. The iCON@QPBI anion-exchange membranes achieved a salt adsorption capacity as high as 15.6 mg g^{-1} and charge efficiency of up to 90%, which are 50% and 20% higher than those of the pristine QPBI membrane, respectively. The performance improvement was attributed to the increased ion-exchange capacity (2.4 mmol g^{-1}), reduced area resistance (5.4 Ω cm^2), and enhanced hydrophilicity (water uptake = 32%) of the iCON@QPBI nanocomposite membranes. This was due to the additional quaternary ammonium groups and conductive ion transport networks donated by the iCON materials. The excellent desalination performance of the iCON@polymer nanocomposite membranes demonstrated their potential for use in MCDI applications and alternative electromembrane processes.

Keywords: Membrane capacitive deionization, nanomaterials, covalent organic nanosheets, ion-exchange membranes, water desalination

1. Introduction

Scarcity of freshwater is one of the most pressing issues currently faced by populations worldwide. According to the water development report of the United Nations, the availability of clean water will worsen in the next 15 years. Desalination technologies such as reverse osmosis (RO), electrodialysis (ED), multistage flash distillation, and mechanical vapor compression have been widely applied in an attempt to alleviate worldwide water shortages [1]. Unfortunately, the high energy consumption and maintenance costs of current commercial desalination technologies have so far limited their widespread application [2]. Capacitive deionization (CDI) has emerged as a technology that can operate at ambient temperatures, atmospheric pressures, and low voltages. Desalination is achieved by applying voltage between two porous electrodes. The electrodes are regenerated by zeroing or reversing the voltage, causing ions to be desorbed from the electrode pores [3]. This has led to the exploration of CDI as a potential low-energy alternative to RO, especially for brackish water [4]. These factors, coupled with the ability to regenerate electrodes, afford the possibility of modular desalination devices with long lifetimes [5]. Further, the ability to recover “contaminant” ions during electrode regeneration indicates that CDI can contribute to a circular water economy [6]. Overall, CDI has demonstrated the ability to meet the requirements of a low-cost environment-friendly route toward clean water. Despite CDI’s ability to remove a wide variety of ions from contaminated water [7], CDI electrodes often suffer from limitations such as low charge and process efficiency due to parasitic redox reactions occurring at the electrode surface [8]. The constant diffusion of ions into the feed stream in a membrane-free CDI technology is a detrimental phenomenon that reduces the overall salt removal and efficiency of the desalination process. By contrast, membrane capacitive deionization (MCDI) uses ion-selective barriers over the electrodes to limit co-ion expulsion back into the feed stream. The retention of co-ions within electrode pores in MCDI attracts more salt ions across the electrode-membrane interface, allowing the electrode pores to remain electroneutral [9]. This markedly increases the net salt removal in MCDI, compared with CDI. Furthermore, effective ion-exchange membranes (IEMs) can mitigate degrading electrode reactions, providing a barrier to prevent the electrode material contacting the feed solution [10]. This increases the charge efficiency and improves

device lifetime. Commercial anion-exchange membranes (AEMs) and cation-exchange membranes (CEMs) have been used extensively for MCDI application [11, 12]; however, these membranes suffer from drawbacks such as high thickness and resistance and low ion-exchange capacity (IEC). All these factors can hinder the performance of MCDI.

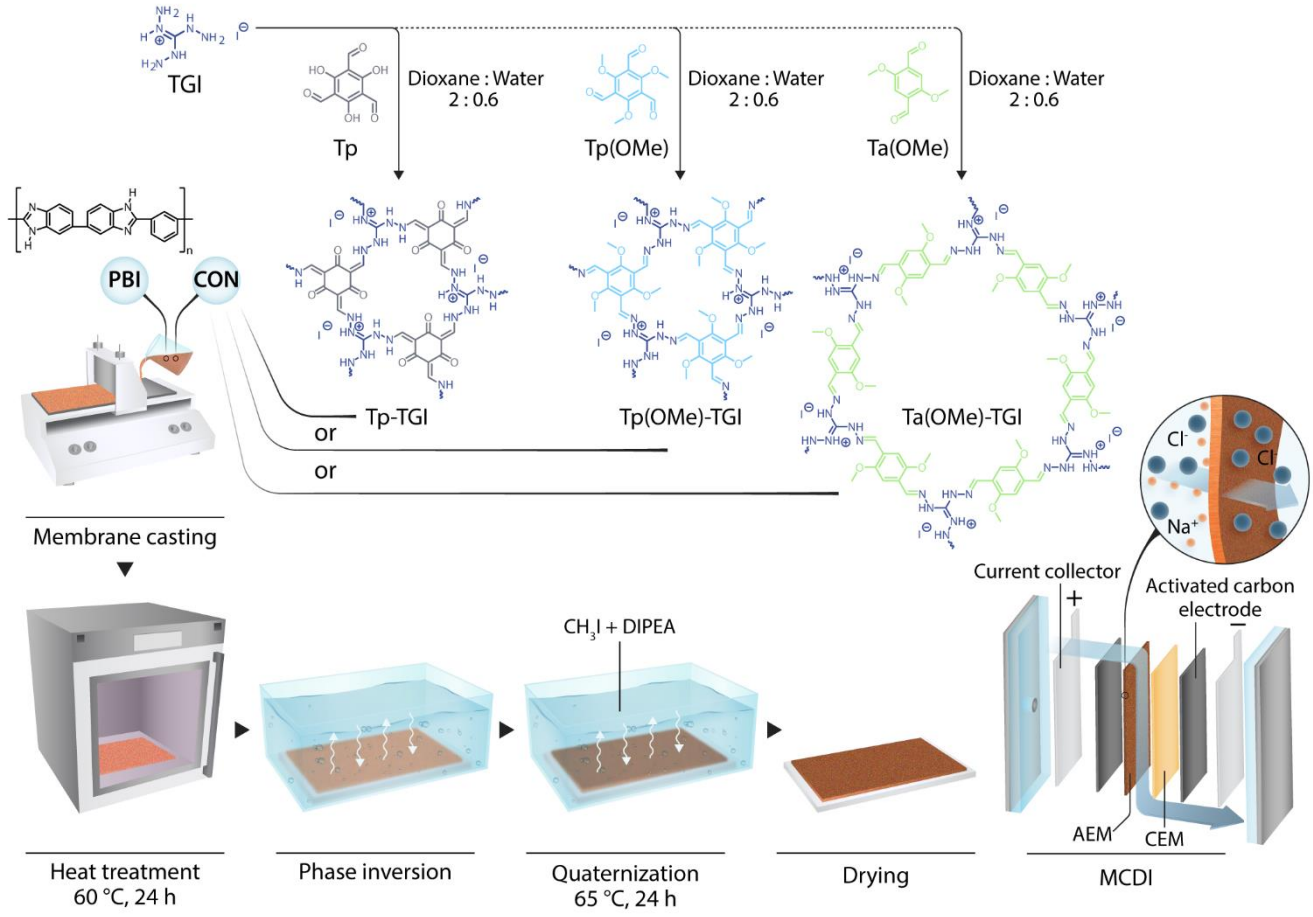

Figure 1. Schematic of the preparation of both the ionic covalent organic nanosheet (iCON) materials and nanocomposite membranes used for membrane capacitive deionization in this study.

Nanomaterials such as graphene [13], molybdenum disulfide (MoS_2) [14], and metal-organic frameworks (MOFs) [15] have been extensively studied as CDI electrode materials owing to the features such as high porosity and surface area for ion adsorption. However, the use of nanomaterials in IEMs for MCDI

is considerably less widespread. Nevertheless, they remain strong candidates to augment the performance of IEMs owing to their unique functional, mechanical, and electrical properties [16]. Nanocomposite AEMs that incorporated reduced graphene oxide/polyaniline (rGO/PANI) have been prepared for MCDI applications [17]. This study demonstrated that the addition of rGO increased the conductivity of the membranes, improving the salt removal efficiency compared with the membranes without the nanomaterial. Moreover, sulfonated graphene oxide (sGO) has been exploited as a stand-alone membrane for MCDI; the CEM was assembled via the dip coating of carbon nanofibers (CNF) into sGO solution [18]. Because of the additional ion-exchange groups and hydrophilic nature of the sGO material, the sGO/CNF composite was able to nearly double the salt removal and charge efficiency compared with the pristine CNFs. An innovative atomic layer deposition method was used to deposit titanium oxide (TiO_2) particles onto the CNT membrane electrodes [19]. The TiO_2 layer more than doubled the electrosorption capacity of the CNT membrane electrodes relative to the pristine electrodes, which was attributed to the hydrophilic layer facilitating the transport of a greater number of ions into the electrode pores. These studies demonstrate the beneficial effect of incorporating nanomaterials into IEMs for MCDI.

Covalent organic nanosheets (CONs) are an alternative family of nanomaterials comprising organic linkers that are symmetrically covalently bonded to form a two-dimensional (2D) network [20]. Considerable efforts have been made in recent years to advance the preparation of covalent organic framework materials, especially in the monolayer form or few-layered CONs [21, 22]. CONs are attractive candidates for functional materials to be used in (M)CDI and other water remediation processes owing to their material characteristics such as high surface area, porosity, nanoscale channels, and chemical stability [23]. Further, the CON's few-layered structure and organic nature make them amenable to predesigned functionalization. Recently, a redox-active CON was prepared for use as a CDI electrode [24]. This material provided a high capacitance and achieved a high salt-adsorption capacity owing to the redox-active nature of the CON and high porosity for maximum ion removal. The possibility to further modify the CONs with charged species makes them ideal additive materials for nanocomposite IEMs. The incorporation of

functional nanomaterials (with ionic charge) into a polymer matrix has previously been shown to increase the IEC and conductivity of IEMs [25]. The improvement of these membrane properties can considerably enhance salt removal and charge efficiency of the MCDI process [26]. Recently, CONs with a positive charge (quaternary ammonium) have been added to brominated poly(2,6-dimethyl-1,4-phenylene oxide) (PPO) polymer to prepare membranes with enhanced hydroxide conductivity for AEM fuel cells [27].

In this work, for the first time, we demonstrate the loading of ionic CONs (iCONs) into a polymer matrix of quaternized polybenzimidazole (QPBI), to prepare AEMs tailored for MCDI applications. The complete preparation procedure is outlined in Figure 1. The introduction of guanidinium-linked iCONs with built-in positive charge was hypothesized to increase the IEC and conductive transport pathways within the QPBI membranes. When this membrane is used in MCDI, these factors have the potential to improve the desalination performance. The iCON@QPBI AEMs' surface, hydrophilic, thermal, and electrochemical properties were determined and compared with those of a pure QPBI membrane (without the addition of iCON). When compared with QPBI polymer membranes and similar ion-exchange materials reported in the literature, the iCON@QPBI membranes with an in-built positive charge were able to increase the salt removal and charge efficiency of the MCDI process. This performance improvement was attributed to the introduction of the iCON materials, which imparted additional functionality and a greater number of ion-transport pathways throughout the polymer matrix of the membranes.

2. Experimental Section

2.1. Materials. Poly[2,2'-(*m*-phenylene)-5,5'-bisbenzimidazole] (PBI) dope solution (26 wt% in *N*-*N*-dimethylacetamide (DMAc)) was purchased from PBI Performance Products (Charlotte, NC, USA). Iodomethane (MeI, >99%), *N,N*-diisopropylethylamine (DIPEA, >98%), sodium chloride (NaCl, >99%), and 1-methyl-2-pyrrolidone (NMP, 99%) were purchased from Sigma-Aldrich. DMAc (>99.5%) and potassium nitrate (KNO_3, >99%) were purchased from Acros. Acetonitrile (CH_3CN, >99.5%) and silver nitrate ($AgNO_3$, 99.7%) were purchased from Fisher-Scientific. Activated carbon (YEC-8A) was obtained from Fuzhou Yihuan Carbon Company. Carbon black (CB, Super P) conductive additive was purchased from

Alfa Aesar. Poly vinylidene fluoride (PVDF, Kynar 761) binder was purchased from Arkema, and graphite current collectors (99%) were purchased from Gee Graphite Ltd.

2.2. iCON Fabrication. A solvothermal Schiff-base condensation reaction between 0.2 mmol of triaminoguanidinium iodide (**TGI**) and 0.2 mmol of respective trialdehydes (1,3,5-triformylphloroglucinol [**Tp]** [28], 1,3,5-triformyl-2,4,6-trimethoxybenzene [**Tp(OMe)]**, and 2,5-dimethoxy-1,4-terephthaldehyde [**Ta(OMe)**]) in dioxane:water (1:1 v/v) was performed in a vacuum sealed Pyrex tube heated at 120 °C for 72 h to produce the three iCONs i.e., **Tp–TGI**, **Tp(OMe)–TGI**, and **Ta(OMe)–TGI**, respectively (see supporting information (SI)). The obtained iCONs were washed sequentially with hot DMAc and water to remove any residual starting material or oligomers. Prior to characterization studies, the iCONs were washed with water and then with acetone before being dried under vacuum at 90 °C for several hours.

2.3. Electrode Preparation. Porous carbon electrodes were prepared using a slurry comprising activated carbon powder, CB, and PVDF binder (8:1:1 ratio) in NMP solvent. The slurry was coated onto a graphite current collector using a doctor blade with an air gap of 800 μm and annealed in a vacuum oven at 90 °C for 12 h. The final electrodes had an approximate area of 1 cm^2 and mass loading between 9–12 mg cm^{-2}.

2.4. Membrane Preparation. iCON@QPBI nanocomposite membranes were prepared using the solution casting method. A given mass of iCON was initially dispersed in 1 mL of DMAc via sonication for 1 h. The iCON suspension was added to 0.77 g of PBI solution (26 wt% in DMAc, 0.2 g of polymer) and mechanically stirred (80 rpm) at 60 °C for 12 h. The final polymer concentration of all dope solutions was 10 wt%. The dope solution was degassed using an incubator shaker (30 °C; 300 rpm) for 12 h and blade coated (air gap of 200 μm) onto a clean glass plate using an Elcometer 4340 film applicator. The film was dried at 60 °C for 12 h before being precipitated by immersion in deionized (DI) water, causing the membrane to peel away from the glass plate. The PBI polymer was quaternized within the membrane via methylation using MeI, as outlined in our previous work [29]. Anion substitution of the membranes was initiated by soaking them in NaCl solution (1 M) for 48 h to prepare them for desalination application (chloride form). Six membranes were prepared in total, designated iCON@QPBI-x, where iCON refers

to the identity **Tp–TGI**, **Tp(OMe)–TGI**, and **Ta(OMe)–TGI** and *x* is the total mass percentage of iCON in the membrane (*x* = 2.5, 5, and 10).

2.5. Membrane Characterization. Surface and cross-sectional scanning electron microscopy (SEM) and energy dispersive X-ray (EDX) images of membrane samples were obtained using an FEI Quanta 250 ESEM instrument. Membranes were sputtered with Pt coating (10 nm) prior to imaging for enhancing image resolution. Thermal stability of membranes was analyzed via thermogravimetric analysis (TGA) using a TA Instruments Q500 under N_2 atmosphere. Water-in-air contact angle measurements were performed using a Kruss Drop Shape Analyzer (DSA 100 Instrument) with a droplet volume of 1.5 µL. Water uptake (WU) and linear swelling ratios (LSR) were obtained using the following equation:

$$\text{WU (\%)} = \frac{m_w - m_d}{m_d} \times 100\% \quad (1)$$

$$\text{LSR (\%)} = \frac{L_w - L_d}{L_d} \times 100\% \quad (2)$$

where m_w, m_d, L_w, and L_d are the hydrated mass, dry mass, hydrated length, and dry lengths of the membrane pieces, respectively. Hydrated masses and lengths of the membrane pieces were obtained after their immersion in DI water for 24 h and dry masses and lengths were recorded after drying them in a vacuum desiccator for 24 h. IECs were measured using Mohr's titration method [30] with $AgNO_3$ (0.01 M), in a manner similar to a previous work [29]. Contact angle, WU, LSR, and IEC measurements were performed in triplicate for all membrane samples. Area resistance (R_A) values for membranes were determined via electrochemical impedance spectroscopy (EIS) using a potentiostat (Metrohm, Autolab) equipped with a frequency response analyzer (FRA32M). A two-electrode sandwich setup was employed with Pt mesh electrodes and 1 M NaCl electrolyte in each compartment Impedance measurements were conducted using an alternating current signal with 0.1-mA amplitude in the frequency range of 1 Hz–1 MHz. The resistance of the membrane in 1-M NaCl solution (R_{MS}) was calculated through Bode modulus plots and normalized by the exposed membrane area (A = 0.2 cm^2) using the following equation:

$$R_A = (R_{MS} - R_S)A \quad (3)$$

where R_S is the solution resistance of 1-M NaCl. Detailed explanation and interpretation of the EIS measurements can be found in the SI.

2.6. MCDI Desalination Tests. The flow-between MCDI cell comprises an iCON@QPBI nanocomposite as the AEM and a commercial CEM (Fumasep FKS-50) placed over the anode and cathode, respectively. Membranes were conditioned in the electrolyte (NaCl, 200 mg l^{-1}) for 24 h prior to the experiments and the anode and cathode were AC/CB/PVDF (8:1:1) electrodes for all MCDI tests. The electrodes were separated using an acrylic spacer (width = 1 mm) to create a water flow channel. MCDI desalination was conducted in a batch mode where the effluent water was recycled into the feed reservoir. The feed electrolyte (NaCl, 200 mg l^{-1}) was purged with Ar (30 min) and pumped through the MCDI cell using a peristaltic pump (VWR) at a flow rate of 5 mL min^{-1}. The system was cycled for 10 adsorption/desorption (1.2 V/0.0 V) cycles for 1 h, followed by at least 5 adsorption/desorption cycles for 2 h. This verified the cycling stability of the system over >40 h of continuous operation. The desalination was monitored using a conductivity meter (Seven Excellence, Mettler Toledo), and voltages were applied using a potentiostat (Metrohm, Autolab). Conductivity values (µS cm^{-1}) were converted to salt concentration (mg L^{-1}) via a calibration plot using a reference temperature of 25 °C. MCDI performance was quantified via salt-adsorption capacity (SAC), charge efficiency (Λ), average salt-adsorption rate (ASAR), and energy normalized to adsorbed salt (ENAS) given by

$$SAC\ (mg\ g^{-1}) = \frac{(C_0 - C_{eff})V_s}{m_e} \quad (4)$$

$$\Lambda\ (\%) = \frac{(C_0 - C_{eff})V_s F}{MQ} \times 100\% \quad (5)$$

$$ASAR\ (mg\ g^{-1}\ min^{-1}) = \frac{SAC}{t} \quad (6)$$

$$ENAS\ (\mu mol\ J^{-1}) = \frac{(C_0 - C_{eff})V_s}{ME_{ads}} \quad E_{ads} = V \int I dt \quad (7)$$

where C_0, C_{eff}, V_s, and m_e are the initial concentration (mg l^{-1}), effluent concentration (mg l^{-1}), reservoir volume (l), and electrode mass (g), respectively. F is the Faraday constant (96 485 C mol^{-1}), M is the

molar mass of NaCl (58.5 g mol^{-1}), Q is the charge supplied per adsorption cycle (C), t is the duration of the adsorption cycle (min), and E_{ads} is the energy supplied during an adsorption cycle during constant voltage MCDI. Average values of each of these parameters was calculated from the respective values of at least five cycles when the MCDI system had attained equilibrium.

3. Results and Discussion

3.1. iCON Characterization. As-synthesized **Tp–TGI**, **Tp(OMe)–TGI**, and **Ta(OMe)–TGI** iCONs comprise guanidinium units (**TGI**) and three different trialdehdyes i.e., **Tp**, **Tp(OMe)**, and **Ta(OMe)**, respectively, as shown in Figure 1. The cationic charge present in the framework structure has been exclusively inherited from the guanidinium linker unit. In the powder X-ray diffraction (PXRD) pattern of **Tp–TGI**, the first peak displayed at 2θ = 9.43° corresponds to the [100] plane, as shown in Figure 2. The breadth of this peak indicates low crystallinity of the as-synthesized **Tp–TGI** iCON.

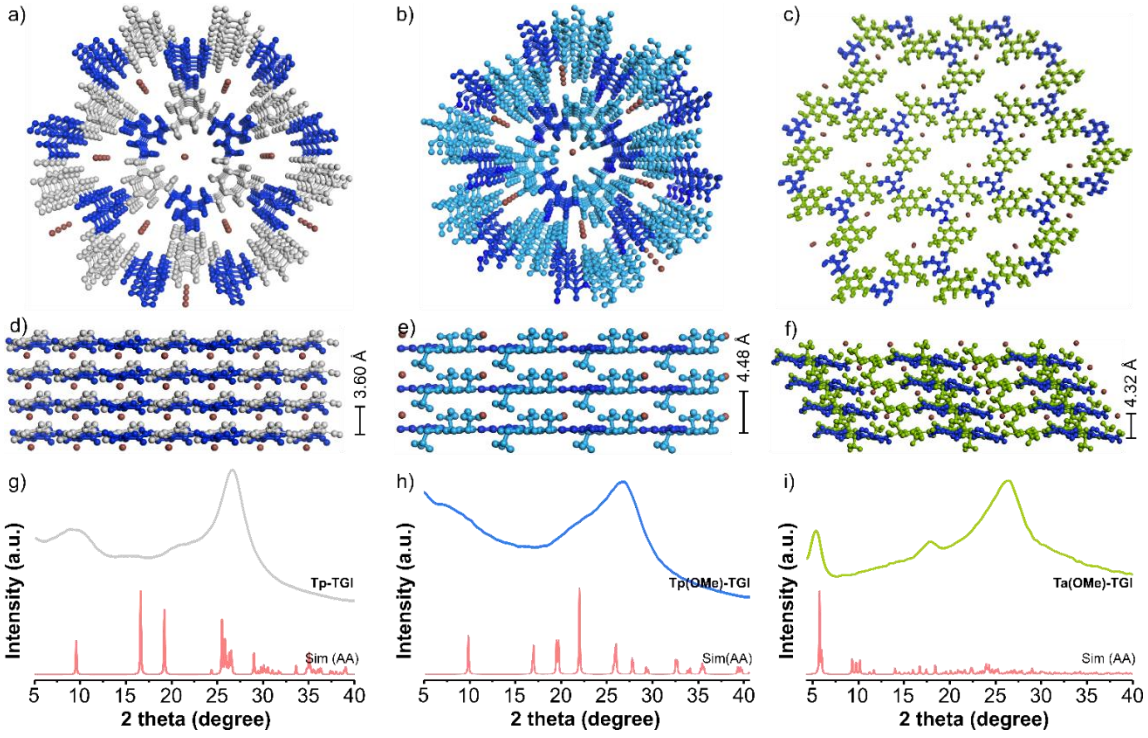

Figure 2. Structural representation of eclipsed AA stacking model of a) **Tp–TGI**, b) **Tp(OMe)–TGI**, and c) **Ta(OMe)–TGI** iCONs. Color assignment: **Tp** is shown in light gray, **Tp(OMe)** in light blue, **Ta(OMe)** in

green, **TGI** in dark blue, and counter iodide ion in brown. d–f) Side views demonstrate the distance between the two adjacent layers of the corresponding iCONs. g–i) Comparison of the PXRD patterns among the as-synthesized g) **Tp–TGI** (gray), h) **Tp(OMe)–TGI** (light blue), and i) **Ta(OMe)–TGI** (green) iCONs against the simulated eclipsed (AA) model.

However, in the case of **Tp(OMe)–TGI**, the first peak is broader than the corresponding peak for **Tp–TGI**. An intense broad peak exists at 2θ = 26.68° (for **Tp–TGI**) and 26.40° (for **Tp(OMe)–TGI**), indicating the existence of weak π–π interactions between the adjacently stacked iCON layers. In the case of **Ta(OMe)–TGI**, the first peak appears at 2θ = 5.05° corresponding to the [100] plane and the peak at 2θ = 26.29° corresponds to the [001] plane. According to a previous report [28], the presence of inherent cationic character within the guanidinium unit and the presence of iodide counter anion in the framework structure act to weaken the π–π interactions between the adjacent iCONs. This is also considered responsible for the intrinsic self-exfoliation of the framework structure, resulting in the structure's low crystallinity. Moreover, this self-exfoliation reduces the material's overall porosity, which may result in a low surface area and nonuniform pore-size distribution. However, these weak π–π interactions are favorable for dispersing the material in organic solvents, which is required for use of the iCON as filler particles in nanocomposite membranes.

To elucidate the structure of the prepared iCONs, eclipsed (AA) and staggered stacking models were simulated (Figures S11–S16, SI). Monolayer models of each iCON were built using either the hcb (**Tp–TGI** and **Tp(OMe)–TGI**) or hca (**Ta(OMe)–TGI**) nets. Monolayers were optimized using the universal force field. Before eclipsed (AA), slip-stacked and staggered (AB) bilayer models were optimized using the density-functional tight-binding method with the 3ob-3-1 parameters. All calculations were performed in AMS [31]. For **Tp–TGI**, the XRD pattern was in agreement with the eclipsed AA model, as shown in Figure 2g. The fitting parameters obtained after Pawley refinement are R_{wp} = 4.52% and R_p = 3.34%, and the lattice parameters are as follows: a = 10.746 Å, b = 10.758 Å, c = 3.454 Å, α = 90.04°, β = 89.233°, and γ = 120.56° (see SI for refinement fitting parameters of **Tp(OMe)–TGI** and **Ta(OMe)–TGI**).

According to the simulated structure of **Tp–TGI**, the distance between two adjacent layers is calculated to be approximately 3.60 Å, with an iodide ion situated between the two layers. Meanwhile, in the case of **Tp(OMe)–TGI**, the interlayer spacing distance is calculated as 4.48 Å, which is slightly greater than that of **Tp–TGI**. This could be attributed to the presence of iodide ions as well as the methoxy groups between the two adjacent layers. In the case of **Ta(OMe)–TGI**, the distance between two adjacent layers is approximately 4.32 Å, which is 0.72 Å greater than that in **Tp–TGI** and 0.16 Å smaller than that in **Tp(OMe)–TGI**.

In the Fourier transform infrared (FTIR) spectra of the as-synthesized **Tp–TGI** and **Tp(OMe)–TGI** iCONs, the bands observed at ~1574 and 1610 cm^{-1} (for **Ta(OMe)–TGI**) are assigned to the characteristic C=C stretch and the stretching band at ~1280 cm^{-1} is assigned to the C–N bonds (Figures S2–S4, SI). In addition, the disappearance of the characteristic C=O peak (1634 cm^{-1}) of aldehyde and primary amine of the guanidinium precursor indicates complete consumption of the starting materials. The solid-state ^{13}C CP-MAS NMR spectroscopic studies were performed to determine the structure of the as-synthesized iCONs in a crystalline state (Figures S5–S7, SI). The structure for the **Tp–TGI** iCON is in agreement with the reported study [28]. For **Tp–TGI** iCON, the sharp peak seen at 100 ppm was assigned to the carbon atom adjacent to the carbonyl carbon atom. The signal at 150 ppm was assigned to the carbon atom bonded to the nitrogen atom of the guanidinium unit. A low-intensity peak appeared at 192 ppm, which was assigned to the characteristic C=O carbon and strongly indicated the existence of the keto-form of the as-synthesized **Tp–TGI** iCON [22]. On a similar line, the ^{13}C NMR spectra of **Tp(OMe)–TGI** and **Ta(OMe)–TGI** are straightforward to interpret; the characteristic peaks for the methoxy group appear at 35 and 57 ppm, respectively (For details see SI). All three iCONs are stable up to a temperature of 200 °C, as evidenced by the TGA profiles. (Figure S8, SI). Analysis of SEM images substantiate the existence of as-synthesized iCONs as micrometer-sized sheets, and the corresponding EDX profiles show that C, N, O, and I elements are the major components of the prepared iCONs (Figures S22–S24, SI).

The N_2 adsorption isotherms of all three activated iCONs were measured at 77 K and all three iCONs displayed a type-II reversible adsorption isotherm. The Brauner–Emmett–Teller (BET) surface areas for the as-synthesized **Tp–TGI**, **Tp(OMe)–TGI**, and **Ta(OMe)–TGI** iCONs were calculated as 287, 296, and 313 $m^2 g^{-1}$, respectively (Figure 3). Weak π–π interactions between adjacent layers, small pore size, and the presence of iodide ions within the structure were the most probable factors responsible for the low surface area values. The nonlocal density functional theory (NLDFT) was used to calculate the pore-size distributions of all three iCONs. A wide range of pore diameters was observed in a pore-size distribution profile (Figures S25–S27, SI). This could be attributed to the lack of a proper channeled structure and the iodide-ion assisted blocking of pores. These observations are consistent with the literature where the exfoliation of 2D layers led to a loss in the finite porosity of the resulting nanosheets [22].

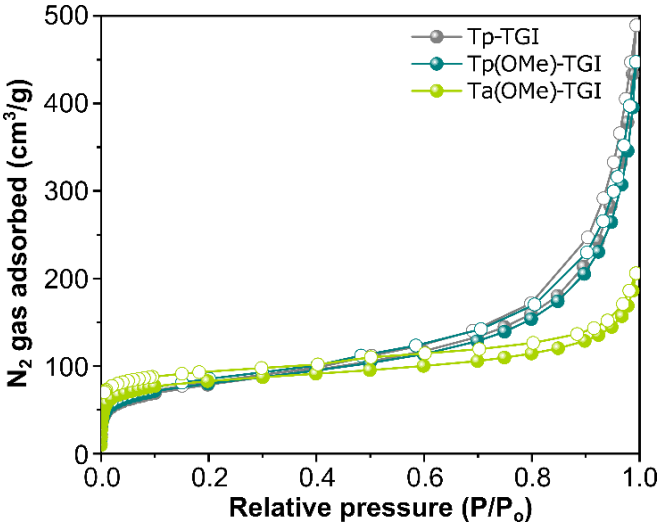

Figure 3. Nitrogen gas uptake isotherm for the **Tp–TGI**, **Tp(OMe)–TGI**, and **Ta(OMe)–TGI** iCONs recorded at 77 K.

As-synthesized iCONs were found to form a stable aqueous dispersion when immersed in water for 3 d; the formation of a stable colloidal suspension was further verified via the typical Tyndall effect (Figure S31, SI). Chemical stability of the iCONs was assessed by their immersion in different solvents such as aqueous HCl (3 M), aqueous NaOH (3 M) solution, DMAc, methanol (MeOH), water, and tetrahydrofuran

(THF) for 7 d (Figures S33 and S34, SI). Analysis of PXRD patterns and FTIR spectra substantiate the high stability of these iCONs in all these solutions except in the alkaline medium (Figure S35 and S36, SI).

As previously mentioned, porosity and conductivity are considered as two important properties that contribute to the selection of the ICONs as electrode materials for use in the CDI process. Owing to the interfacial nature of ion electrosorption, these porous iCON materials can facilitate maximum contact between membrane surface and the feed saltwater stream when incorporated into a polymer membrane. This condition could increase the membrane wettability and expedite ion transport through the AEM into the electrode pores, improving its MCDI performance. It has previously been found that because of a weak electric double-layer overlap, materials comprising mesopores were preferred over the microporous structure [32, 33]. Subsequently some microporous materials such as activated carbons[34, 35] and carbide-derived carbons [36] were found to be more efficient toward desalination and thus were preferred over mesoporous analogs. **Tp–TGI**, **Tp(OMe)–TGI**, and **Ta(OMe)–TGI** iCONs are microporous in nature. However, the presence of positive charge inherited from the guanidinium unit, leading to their self-exfoliation, has resulted in a nonuniform pore-size distribution in the framework structure.

3.2. Membrane Characterization. The membrane surface and cross-sectional morphologies were examined using SEM imaging. Representative SEM and EDX images are displayed in Figure 4, and complete SEM images for all membranes are displayed in Figure S39 (SI). The comparison of surface images of QPBI (Figure 4a) and **Tp–TGI@QPBI-10** (Figure 4b) highlight the effect of iCON loading into the polymer matrix. The addition of 10 wt% of iCON to the polymer resulted in an increase in the number of surface features and undulations compared with the pristine QPBI membrane surface. This is reinforced by the full SEM images (Figure S39, SI), which show an increasing number of surface features as the iCON loading is increased up to 10 wt%. The cross-sectional SEM images (Figure S37, SI) show a dense and nonporous ion-exchange film formed during phase inversion for all the nanocomposite AEMs. Cross-sectional thicknesses (Table 2) were between 22–25 μm for all the membrane samples. EDX mapping of oxygen distribution across the membrane surface is displayed in Figures 4c and 4d. As the QPBI

polymer contains no oxygen-bearing functionalities, any EDX signals due to oxygen were assigned to the iCON. The EDX map shows a uniform distribution of oxygen across the surface, indicating the thorough mixing of iCON and polymer phases during the preparation process. The oxygen EDX map of QPBI (Figure 4c) shows negligible oxygen intensity; thus the small signals were assigned to residual water within the membrane after drying. This confirmed the successful embedding of iCON into the polymer matrix. The organic nature of the iCON filler ensured its good compatibility with the PBI polymer phase. This ensured a higher mass loading into the polymer matrix (10 wt%) compared with the similar PBI nanocomposite membranes prepared using fillers such as graphene or graphene oxide [37]. The uniform distribution of iCON throughout the polymer matrix can provide chloride-ion-transport pathways via quaternary ammonium groups within the iCON framework. Overall, the membranes showed promising morphological characteristics to be used as IEMs in MCDI.

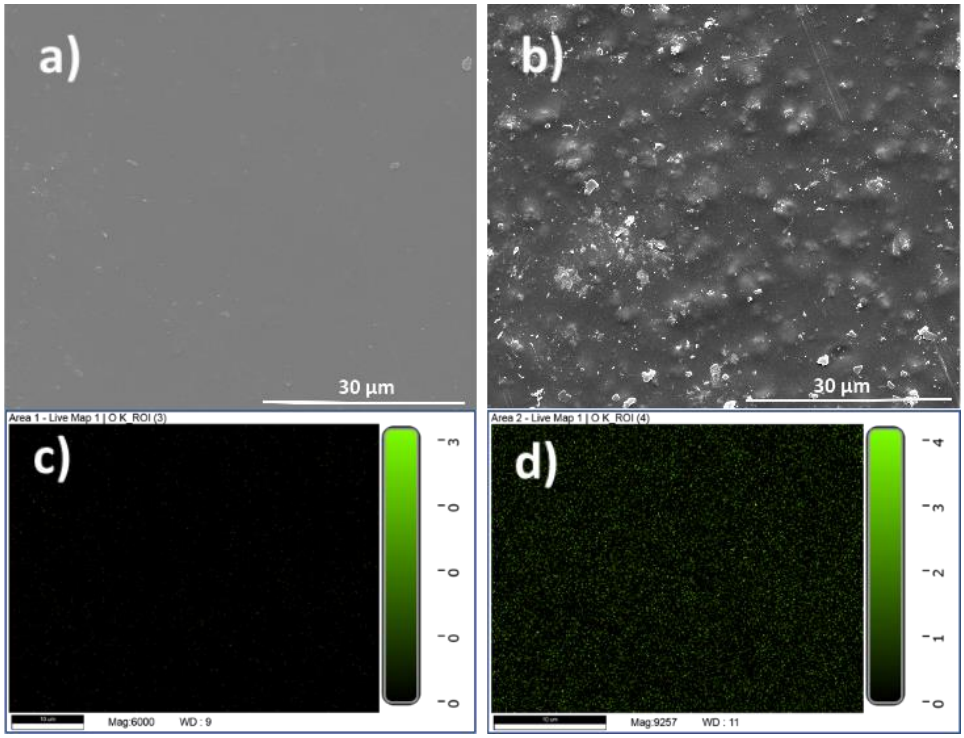

Figure 4. Representative surface SEM images and oxygen EDX map of (a and c) QPBI and (b and d) **Tp–TGI@QPBI-10** AEMs.

Thermal properties of the nanocomposite IEMs were determined using TGA analysis. Decomposition curves for all membranes are displayed in Figure S41 (SI). All membranes displayed high thermal stability up to 250 °C. Although the iCON membranes with a mass loading of 5–10 wt% displayed more accelerated decomposition than that of QPBI, all membranes retained ~80% of the initial mass up to T = 600 °C. This is partially due to the excellent thermal stability of PBI polymer [38], and the thermal properties of membranes were not sacrificed by the addition of iCON to the polymer matrix.

Hydrophilicity and wettability characteristics of the iCON@QPBI membranes were determined via water-in-air contact angle measurements as well as WU and LSR. The results are presented in Table 1 and full contact angle images are displayed in Figure S40 (SI).

Table 1. Selected hydration and dimensional properties of iCON@QPBI anion-exchange membranes. Thickness values were determined using ImageJ software and taken as an average of at least three separate measurements.

	Contact Angle (°)	Water Uptake (%)	Linear Swelling Ratio (%)	Thickness (μm)
QPBI	65.1 ± 1.6	20.6 ± 6.9	5.6 ± 1.0	23.0 ± 0.8
Tp–TGI@QPBI-2.5	61.8 ± 1.5	21.1 ± 3.5	10.3 ± 1.6	23.5 ± 0.5
Tp–TGI@QPBI-5	61.5 ± 0.3	27.4 ± 2.1	7.9 ± 4.0	22.0 ± 0.3
Tp–TGI@QPBI-10	58.4 ± 1.7	31.1 ± 2.4	7.1 ± 0.5	23.1 ± 0.8
Ta(OMe)–TGI@QPBI-10	59.8 ± 0.3	30.0 ± 6.7	6.9 ± 0.7	23.5 ± 0.4
Tp(OMe)–TGI@QPBI-10	53.7 ± 2.0	32.2 ± 1.6	11.4 ± 1.3	24.3 ± 0.4

The measured contact angle for all the examined membranes was <90°, indicating a hydrophilic surface that is suitable for water desalination [39]. Notably, increasing mass loading of iCON into the QPBI matrix increases the hydrophilicity and wettability of the membrane surface. This is evidenced by a gradual decline in contact angle from QPBI (65°) to values in the range of 54°–60° for 10 wt% of iCON loading.

The **Tp(OMe)–TGI@QPBI-10** membrane exhibited the highest hydrophilicity with a contact angle of 54° and a corresponding WU of 32%. The reduction in the contact angle with iCON loading can be rationalized by the increasing number of oxygen atoms arising from the functional groups of the various iCONs. The alcohol, aldehyde, and methoxy groups present in the iCON frameworks (Figure 1) contribute the oxygen atoms that get embedded in the QPBI backbone, which is more hydrophobic in nature. These oxygen-containing functionalities can form hydrogen bonds with water droplets suspended on the membrane surface, thereby improving the surface hydrophilicity and reducing the contact angle [40]. The reduction in the contact angle is accompanied by an increase in WU for membranes as the mass loading of iCON increases. The WU values (20%–32%) match closely with the values for commercial IEMs used in water treatment processes [41]. The increased hydrophilicity and WU of the membrane has the potential to improve ionic conductivity and the subsequent ion uptake and storage in the carbon electrode. It has previously been reported that carbon electrodes coated with a polydopamine (PDA) layer increased SAC owing to the hydrophilic PDA facilitating ion transport into the electrode pores [42]. Furthermore, all membranes demonstrated limited swelling in aqueous environments, with LSR values in the range of 5–11 wt%. These hydrophilic and dimensional properties imply that the membranes could be used effectively in MCDI.

3.3. Electrochemical Characterization. Electrochemical characteristics of the iCON@QPBI membranes may considerably affect the final salt removal and charge efficiency of the MCDI process. The IEC of an IEM represents the number of functional groups that contribute to counterion (chloride) transport. A membrane with high IEC is beneficial to MCDI desalination because more ions can be removed from the feed stream. The IEC results are displayed in Figure 5. The measured IEC values in this study (1.9–2.4 mmol g^{-1}) exceeded the typical values of the commercial IEMs [41]. QPBI displayed the lowest IEC (1.86 mmol g^{-1}), which matched closely with the previously reported values for QPBI nanocomposite membranes [37]. The addition of iCON led to a noticeable improvement in the IECs for all membranes. For the **Tp–TGI@QPBI** membrane series, the increase of mass loading from 2.5 to 10 wt%

resulted in a steady increase of IEC up to a maximum value of 2.42 mmol g^{-1} for the **Tp–TGI@QPBI-10** membrane. This observation was crucial as it demonstrated the contribution of the iCON to the IEC, in addition to that of the QPBI polymer. Identical quaternization conditions were employed for each membrane, thus any differences in IECs were attributed to the functional groups and counterions donated by the guanidinium linker unit within the iCONs. Moreover, **Ta(OMe)–TGI@QPBI-10** (2.32 mmol g^{-1}) and **Tp(OMe)–TGI@QPBI-10** (2.28 mmol g^{-1}) showed noticeable improvement in IECs compared with that of the QPBI membrane, albeit achieving slightly lower values than **Tp–TGI@QPBI-10**. The increase in IEC results for iCON@QPBI membranes is in line with the positive zeta potential values measured for each iCON material (Figure S28–S30, SI). These positive values indicate a material with cationic nature (higher positive charge), which favors their use in AEMs. The zeta potential values of **Ta(OMe)–TGI** (30 mV) and **Tp(OMe)–TGI** (28 mV) indicate a greater cationic nature than **Tp–TGI** (18.4 mV), which could enhance the IECs of AEMs. However, the subsequent embedding of iCONs within the membrane can lead to factors such as ion trapping in the matrix, implying that not all ions contribute to ion-exchange [37]. The IEC results confirmed a successful impregnation of iCON and its ability to increase the IEC of the polymer membrane, which can increase SAC during MCDI desalination.

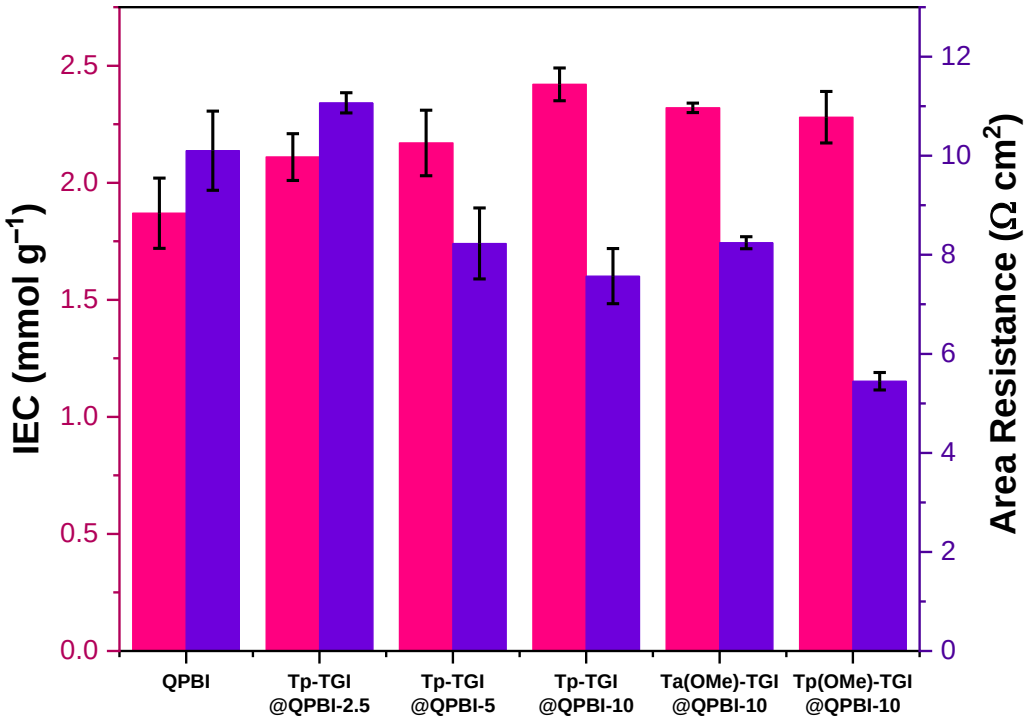

Figure 5. Ion-exchange capacity and area resistance values for iCON@QPBI nanocomposite membranes.

Corresponding area resistance (R_A) values for all iCON@QPBI membranes are displayed in Figure 5. Similar to IEC, the area resistance is a critical electrochemical property that quantifies the resistance to the transportation of ions through an exposed area of the membrane. For MCDI, low R_A values are preferred to facilitate ion transport into the electrode pores, which can in turn improve salt removal and reduce the energy consumption of the system [43]. The Bode magnitude plots obtained from the two-electrode configuration (Figure S37, SI) are displayed in Figure S41 (SI). Resistance values were extracted directly from the high-frequency intercept of these plots (Figure S42a, SI), and the membrane resistance was determined via the difference between the resistance of the membrane immersed in an electrolyte ($\mathbf{R}_{MS}$) and the resistance of a blank cell (R_S, electrolyte only). As depicted in Figure 5, QPBI (10.1 Ω cm^2) and **Tp–TGI@QPBI-2.5** (11.1 Ω cm^2) show similar R_A values, indicating that the membrane resistance is not considerably affected by the low loading of iCON into the QPBI matrix. However, further

loading of **Tp–TGI** into the QPBI matrix decreases the area resistance, producing the values of 8.2 Ω cm^2 and 7.6 Ω cm^2 for **Tp–TGI@QPBI-5** and **Tp–TGI@QPBI-10**, respectively. This trend confirmed the inherent conductivity of the iCON materials, which could incorporate additional ion-transport channels throughout the polymer matrix. This observation was confirmed when examining the other membranes with 10 wt% iCON loading. **Tp(OMe)–TGI@QPBI-10** (5.4 Ω cm^2) achieved the lowest area resistance between all studied membranes, a reduction of almost 50% compared with the area resistance of the pristine QPBI membrane. This result was in agreement with the enhanced WU (32%) of the **Tp(OMe)–TGI@QPBI-10** membrane, which can also contribute to ion conductivity through the membrane. The reduced R_A values of the iCON@QPBI membranes relative to QPBI highlight the ability of the iCONs to augment ion transport through the polymer, owing to the additional ionic groups throughout the QPBI backbone.

3.4. MCDI Performance of iCON@QPBI Membranes. Batch-mode MCDI experiments were performed to determine the desalination capability of each iCON@QPBI membrane. These membranes were used as AEMs and placed adjacent to the anode, with commercial CEM (Fumasep FKS-50) adjacent to the cathode. The conductivity changes over time for each MCDI system are presented in Figure S44 (SI). The profiles presented in this figure display the system's response to applied voltage; all systems displayed the depletion of conductivity during adsorption (1.2 V) and increment during desorption (0 V). This indicates the removal of salt from the feed stream during adsorption and the ability of the electrodes to regenerate after the voltage is removed during each cycle. This confirmed that iCON@QPBI membranes can function as effective ion-exchange barriers, enabling counter-ion transport into the electrodes during adsorption and back into the feed stream during desorption. Consequently, each iCON@QPBI/CEM system received the expected cyclic MCDI response. Furthermore, the profiles shown in Figure S44 were obtained immediately after 10 initial adsorption/desorption cycles (duration 1 h). This highlighted that all MCDI systems could maintain regenerative behavior and desalination performance for more than 40 h of continuous operation. This indicated good membrane and system stabilities under the application of

voltage over repeated cycles. This is an important consideration for any novel electrode or membrane materials for MCDI.

3.5. MCDI Performance of Tp–TGI@QPBI Membranes. Desalination performance for the systems was quantified by the key metrics SAC, charge efficiency, ASAR, and ENAS. The results for the iCON@QPBI membranes are presented in Figure 6. The QPBI membrane was used as a benchmark for this study to which the performance of the iCON-incorporated membranes could be compared. The QPBI system showed modest SAC (10.0 mg g^{-1}) and charge efficiency (71.8%) compared with those of the iCON@QPBI membranes. These results reflected the IEC (1.86 mmol g^{-1}) and R_A (10.1 Ω cm^2) values of the QPBI membrane, which were the lowest and highest, respectively, among the entire membrane series. Examination of the MCDI results for the **Tp–TGI@QPBI** series of membranes allowed the evaluation of the effect of increasing iCON loading into the QPBI matrix on its desalination performance. The SAC results for the **Tp–TGI@QPBI-2.5** (11.1 mg g^{-1}) and **Tp–TGI@QPBI-5** (13.6 mg g^{-1}) showed a steady increase in the SAC relative to the QPBI membrane. This was attributed to the increasing mass loading of iCON, which contributed to additional quaternary ammonium groups and corresponding counterions (chloride). This increased the IECs of the membranes and consequently the number of ions removed per cycle. The **Tp–TGI@QPBI-10** membrane produced the highest performance in terms of SAC (15.6 mg g^{-1}). This equated to over 50% more salt ions being removed per cycle than for the MCDI system employing QPBI as the AEM. This considerable increase was attributed to the improved IEC (2.42 mmol g^{-1}) and reduced area resistance (7.6 Ω cm^2) of the **Tp–TGI@QPBI-10** membrane, which allowed the transport and storage of a greater number of ions with reduced membrane resistance toward ion transport. This reduced area resistance had the largest impact on the charge efficiency metrics of the systems, increasing the charge efficiency to 87.1% for the **Tp–TGI@QPBI-10** system. This implied that a higher ratio of salt ions was adsorbed per unit charge at this highest mass loading of **Tp–TGI**, indicating a reduction in undesirable phenomena such as co-ion expulsion and faradaic reactions in the MCDI cell [44]. Further, the ASAR and ENAS are important parameters that give insight into the kinetics and energy

consumption of the MCDI process. The ASAR of the **Tp–TGI** series of membranes increased with increasing iCON loading, demonstrating that a greater number of salt ions can be removed in a given time period. Similar to the SAC and charge efficiency, **Tp–TGI@QPBI-10** exhibited the highest ASAR (0.13 mg g^{-1} min^{-1}) among the membrane series. The ENAS of the membranes is perhaps the most important metric because it determines the system energy expended to remove one mole of salt ions from the feed stream. The increasing values of ENAS with **Tp–TGI** loading imply that more salt ions are removed per unit of energy input to the MCDI system. Similar to the charge efficiency, increasing ENAS can be attributed to the **Tp–TGI** filler, resulting in a greater number of conductive ion-transport networks throughout the membrane, reducing resistance to the ion transport and electrical losses within the system. The highest ENAS value for the **Tp–TGI@QPBI-10** membrane (7.5 μmol J^{-1}) was comparable to previously determined values for commercial IEMs [43], reinforcing the potential for using **Tp–TGI@QPBI** as AEMs for MCDI systems.

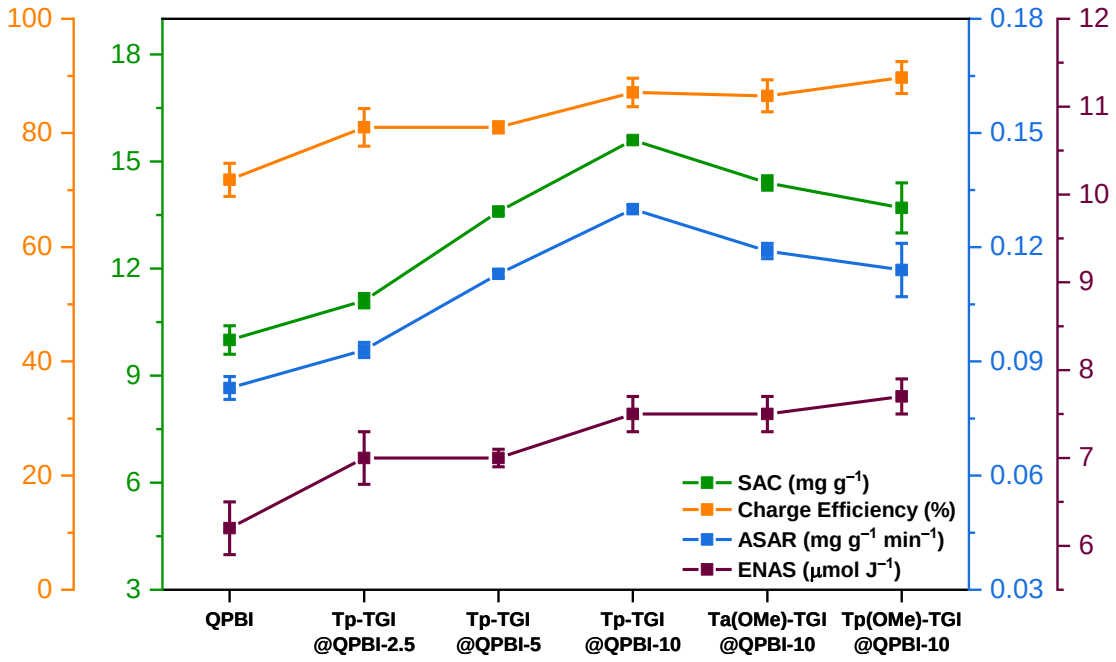

Figure 6. Salt-adsorption capacity (SAC), charge efficiency, average salt-adsorption rate (ASAR), and energy normalized to adsorbed salt (ENAS) values for all nanocomposite iCON@QPBI membranes.

3.6. Comparison of Membranes with different iCON Materials. Following the high desalination performance of the **Tp–TGI@QPBI-10** membrane, two more membranes were prepared using iCON materials (10 wt% mass loading) with different framework configurations. These membranes were denoted by **Ta(OMe)–TGI@QPBI-10** and **Tp(OMe)–TGI@QPBI-10**, and the MCDI results are outlined in Figure 6. This comparison gave insight into whether the material properties of the iCON could influence the MCDI performance. The SAC values of **Ta(OMe)–TGI@QPBI-10** (14.4 mg g^{-1}) and **Tp(OMe)–TGI@QPBI-10** (13.7 mg g^{-1}) were slightly lower than that of **Tp–TGI@QPBI-10** (15.6 mg g^{-1}). This was in agreement with the lower IEC results of the membranes, being 2.32 and 2.28 mmol g^{-1} for **Ta(OMe)–TGI@QPBI-10** and **Tp(OMe)–TGI@QPBI-10**, respectively. This signified fewer salt ions being removed per adsorption cycle during MCDI. Nevertheless, all nanocomposite membranes with 10-wt% iCON loading achieved a higher SAC than the next-best **Tp–TGI@QPBI-5** membrane (13.6 mg g^{-1}), reinforcing the finding that higher iCON loading provides improved MCDI performance. Despite having the lowest SAC among the membranes with 10-wt% iCON loading, the **Tp(OMe)–TGI@QPBI-10** membrane produced the highest values of charge efficiency (89.7%) and ENAS (7.7 μmol J^{-1}) of all MCDI configurations. This reflected the excellent conductive properties of this membrane, with the lowest R_A value (5.4 Ω cm^2) and most hydrophilic character (WU = 32%) among all the tested membranes. These factors expedited ion transport through the membrane into the electrode, enhancing the amount of salt removed per unit of energy supplied to the system. Additionally, the **Ta(OMe)–TGI@QPBI-10** system displayed excellent charge efficiency (86.5%) and ENAS (7.5 μmol J^{-1}), which was comparable to the results achieved using the **Tp–TGI@QPBI-10** membrane. The three iCON frameworks investigated in this study had similar framework structures, varying only slightly in specific factors such as functional groups of precursors (e.g., methoxy) and the number of guanidinium linker units. Therefore, the influence of the type of iCON material on desalination performance, when equivalent mass loadings of each material (10 wt%) are employed, cannot yet be accurately stated. This issue is exacerbated when the iCONs are embedded in the polymer backbone, where specific interactions between the two phases (iCON/QPBI) affect the membrane's properties and subsequent desalination performance. Future research should focus on iCON fabrication using a variety of linkers and framework structures, in order to better understand the influence

of specific iCON frameworks on the MCDI performance. Nevertheless, the study highlighted the potential of iCONs to improve the electrochemical properties of polymer IEMs, which improved their desalination performance when used in MCDI.

The performance of the iCON@QPBI membranes was further validated by their comparison with similar ion-exchange materials that were prepared for MCDI. Comparison results are presented in Table S7 (SI). The iCON@QPBI membranes outperform several similar IEMs regarding both SAC and charge efficiency when a similar feed concentration is employed (200–500 mg L^{-1}). Further, the "R-factor" of the MCDI configuration was determined for the iCON@QPBI membranes and compared with similar ion-exchange materials. This parameter was defined in our previous review and quantifies the ratio of improvement of SAC of the MCDI system compared with that of CDI (without membranes) [45]. This metric enables the comparison between different MCDI systems, regardless of feed salt concentrations and electrode architectures, given that data for both CDI and MCDI are stated. For membranes with 10 wt% iCON loading prepared in this study, the R-factor values were determined to be 3.5, 3.3, and 3.1 for **Tp–TGI@QPBI**, **Ta(OMe)–TGI@QPBI-10**, and **Tp(OMe)–TGI@QPBI-10**, respectively. With both CDI and MCDI data available from the literature, we found these values to be exceeded by only one system (R-factor = 3.7), which employed a novel IEM in MCDI [17]. This reaffirmed the considerable improvement in the desalination performance of the iCON@QPBI AEMs compared with that of the CDI with uncovered electrodes. As mentioned previously, this R-factor can be improved further by optimizing the iCON framework structure with a larger number of quaternary ammonium groups and different linker groups. The optimization of membrane processing should be a focus of future research. This could allow a higher mass loading (>10 wt%) of iCON into the polymer matrix, thereby potentially improving the membranes' desalination performance.

4. Conclusions

In summary, guanidinium-linked iCONs have been fabricated, where a positive charge was inherited from the TGI. The as-synthesized iCONs exhibited chemical stability and porosity and were successfully incorporated into a polymer matrix. To the best of our knowledge, these iCON@QPBI nanocomposite AEMs were used for MCDI application for the first time. When compared with pristine QPBI, the iCON@QPBI membranes showed increased hydrophilicity and improved electrochemical performance with high IEC values of up to 2.4 mmol g^{-1} and low area resistance of 5.4 Ω cm^2. When the iCON@QPBI AEMs were used in conjunction with commercial CEM over the cathode, all MCDI systems demonstrated stability for at least 40 h of operation. The highest SAC (15.6 mg g^{-1}) was achieved using the **Tp–TGI@QPBI-10** membrane, indicating that 50% more salt ions were removed per cycle compared with that using QPBI (without iCON filler). Additionally, charge efficiency (90%) and ENAS (7.7 μmol J^{-1}) values were markedly improved when employing the **Tp(OMe)–TGI@QPBI-10** membrane. These results highlight the beneficial effect of embedding iCONs into a polymer matrix, in order to improve performance in MCDI. We surmise that the increased number of quaternary ammonium groups and ion-transport pathways inherited from the iCONs result in enhanced electrochemical properties of the membranes. This causes increased salt removal, charge efficiency, and reduced energy consumption of all iCON@QPBI configurations compared with those of QPBI. The results from our study show the capability of functional covalent fillers to augment the properties of traditional polymer membranes for improving desalination. This can be applied in future MCDI membrane development and beyond into alternative electromembrane processes such as electrodialysis.

Acknowledgments

The authors would like to thank Jordan Gaskell (University of Manchester) for performing TGA of membrane samples. The authors would also like to thank Athanasios Papaderakis (University of Manchester) for assisting with the EIS measurements. SK thanks the postdoctoral fellowship from the King Abdullah University of Science and Technology (KAUST). The authors acknowledge the UK's Engineering and

Physical Sciences Research Council (EPSRC) under grant code EP/L01548X/1 for funding Robert McNair's doctoral studies through the University of Manchester's Graphene NOWNANO CDT account. Further equipment funding via EPSRC grants EP/S019367/1 and EP/P025021/1 to the Royce Institute are also gratefully acknowledged. The research reported in this publication was supported by funding from KAUST.

References

[1] P.G. Youssef, R.K. Al-Dadah, S.M. Mahmoud, Comparative analysis of desalination technologies, Energy Procedia 61 (2014) 2604–2607.

[2] B. Van der Bruggen, C. Vandecasteele, Distillation vs. membrane filtration: Overview of process evolutions in seawater desalination, Desalination 143 (3) (2002) 207–218.

[3] M.E. Suss, S. Porada, X. Sun, P.M. Biesheuvel, J. Yoon, V. Presser, Water desalination via capacitive deionization: what is it and what can we expect from it?, Energy Environ. Sci. 8 (8) (2015) 2296–2319.

[4] R. Zhao, S. Porada, P.M. Biesheuvel, A. Van Der Wal, Energy consumption in membrane capacitive deionization for different water recoveries and flow rates, and comparison with reverse osmosis, Desalination 330 (2013) 35–41.

[5] E.N. Guyes, A.N. Shocron, Y. Chen, C.E. Diesendruck, M.E. Suss, Long-lasting, monovalent-selective capacitive deionization electrodes, npj Clean Water 4 (1) (2021) 22.

[6] M.S. Mauter, P.S. Fiske, Desalination for a circular water economy, Energy Environ. Sci. 13 (10) (2020) 3180–3184.

[7] R. Chen, T. Sheehan, J.L. Ng, M. Brucks, X. Su, Capacitive deionization and electrosorption for heavy metal removal, Environ. Sci.: Water Res. Technol. 6 (2) (2020) 258–282.

[8] D. He, C.E. Wong, W. Tang, P. Kovalsky, T.D. Waite, Faradaic reactions in water desalination by batch-mode capacitive deionization, Environ. Sci. Technol. Lett. 3 (5) (2016) 222–226.

[9] S. Porada, R. Zhao, A. Van Der Wal, V. Presser, P.M. Biesheuvel, Review on the science and technology of water desalination by capacitive deionization, Prog. Mater. Sci. 58 (8) (2013) 1388–1442.

[10] J. Chang, K. Tang, H. Cao, Z. Zhao, C. Su, Y. Li, F. Duan, Y. Sheng, Application of anion exchange membrane and the effect of its properties on asymmetric membrane capacitive deionization, Sep. Purif. Technol. 207 (2018) 387–395.

[11] J.H. Lee, J.H. Choi, The production of ultrapure water by membrane capacitive deionization (MCDI) technology, J. Membr. Sci. 409–410 (2012) 251–256.

[12] D.I. Kim, P. Dorji, G. Gwak, S. Phuntsho, S. Hong, H. Shon, Effect of brine water on discharge of cations in membrane capacitive deionization and its implications on nitrogen recovery from wastewater, ACS Sustainable Chem. Eng. 7 (13) (2019) 11474–11484.

[13] P. Liu, T. Yan, L. Shi, H.S. Park, X. Chen, Z. Zhao, D. Zhang, Graphene-based materials for capacitive deionization, J. Mater. Chem. A 5 (27) (2017) 13907–13943.

[14] F. Xing, T. Li, J. Li, H. Zhu, N. Wang, X. Cao, Chemically exfoliated MoS2 for capacitive deionization of saline water, Nano Energy 31 (2017) 590–595.

[15] Z. Wang, X. Xu, J. Kim, V. Malgras, R. Mo, C. Li, Y. Lin, H. Tan, J. Tang, L. Pan, Y. Bando, T. Yang, Y. Yamauchi, Nanoarchitectured metal–organic framework/polypyrrole hybrids for brackish water desalination using capacitive deionization, Mater. Horiz. 6 (7) (2019) 1433–1437.

[16] A. Alabi, A. AlHajaj, L. Cseri, G. Szekely, P. Budd, L. Zou, Review of nanomaterials-assisted ion exchange membranes for electromembrane desalination, npj Clean Water 1 (1) (2018) 10.

[17] Y. Zhang, L. Zou, Y. Wimalasiri, J.Y. Lee, Y. Chun, Reduced graphene oxide/polyaniline conductive anion exchange membranes in capacitive deionisation process, Electrochim. Acta 182 (2015) 383–390.

[18] B. Qian, G. Wang, Z. Ling, Q. Dong, T. Wu, X. Zhang, J. Qiu, Sulfonated graphene as cation-selective coating: A new strategy for high-performance membrane capacitive deionization, Adv. Mater. Interfaces 2 (16) (2015) 1500372.

[19] J. Feng, S. Xiong, Y. Wang, Atomic layer deposition of TiO2 on carbon-nanotube membranes for enhanced capacitive deionization, Sep. Purif. Technol. 213 (2019) 70–77.

[20] S.Y. Ding, W. Wang, Covalent organic frameworks (COFs): From design to applications, Chem. Soc. Rev. 42 (2) (2013) 548–568.

[21] D.D. Medina, J.M. Rotter, Y. Hu, M. Dogru, V. Werner, F. Auras, J.T. Markiewicz, P. Knochel, T. Bein, Room temperature synthesis of covalent–organic framework films through vapor-assisted conversion, J. Am. Chem. Soc. 137 (3) (2015) 1016–1019.

[22] S. Kandambeth, A. Mallick, B. Lukose, M.V. Mane, T. Heine, R. Banerjee, Construction of crystalline 2D covalent organic frameworks with remarkable chemical (acid/base) stability via a combined reversible and irreversible route, J. Am. Chem. Soc. 134 (48) (2012) 19524–19527.

[23] Z. Xia, Y. Zhao, S.B. Darling, Covalent organic frameworks for water treatment, Adv. Mater. Interfaces 8 (1) (2021) 2170005.

[24] Y. Li, Z. Ding, X. Zhang, J. Li, X. Liu, T. Lu, Y. Yao, L. Pan, Novel hybrid capacitive deionization constructed by a redox-active covalent organic framework and its derived porous carbon for highly efficient desalination, J. Mater. Chem. A 7 (44) (2019) 25305–25313.

[25] M. Vinothkannan, A.R. Kim, G. Gnana Kumar, D.J. Yoo, Sulfonated graphene oxide/nafion composite membranes for high temperature and low humidity proton exchange membrane fuel cells, RSC Adv. 8 (14) (2018) 7494–7508.

[26] O. ul Haq, J.H. Choi, Y.S. Lee, Anion-exchange membrane for membrane capacitive deionization prepared via pore-filling polymerization in a porous polyethylene supporting membrane, React. Funct. Polym. 132 (2018) 36–42.

[27] J. Chen, M. Guan, K. Li, S. Tang, Novel Quaternary ammonium-functionalized covalent organic frameworks/poly(2,6-dimethyl-1,4-phenylene oxide) hybrid anion exchange membranes with enhanced ion conductivity and stability, ACS Appl. Mater. Interfaces 12 (13) (2020) 15138–15144.

[28] S. Mitra, S. Kandambeth, B.P. Biswal, M.A. Khayum, C.K. Choudhury, M. Mehta, G. Kaur, S. Banerjee, A. Prabhune, S. Verma, S. Roy, U.K. Kharul, R. Banerjee, Self-exfoliated guanidinium-based ionic covalent organic nanosheets (iCONs), J. Am. Chem. Soc. 138 (8) (2016) 2823–2828.

[29] R. McNair, L. Cseri, G. Szekely, R. Dryfe, Asymmetric membrane capacitive deionization using anion-exchange membranes based on quaternized polymer blends, ACS Appl. Polym. Mater. 2 (7) (2020) 2946–2956.

[30] H.W. Doughty, Mohr's method for the determination of silver and halogens in other than neutral solutions, J. Am. Chem. Soc. 46 (12) (1924) 2707–2709.

[31] T.S.R. Rüger, M. Franchini, T. Trnka, A. Yakovlev, E. van Lenthe, P. Philipsen, T. van Vuren, B. Klumpers, S.C.M., Theoretical Chemistry, Crije Universiteit (2021), Amsterdam, The Netherlands, AMS. 1 (2021).

[32] L. Zou, L. Li, H. Song, G. Morris, Using mesoporous carbon electrodes for brackish water desalination, Water Res. 42 (8–9) (2008) 2340–2348.

[33] L. Li, L. Zou, H. Song, G. Morris, Ordered mesoporous carbons synthesized by a modified sol–gel process for electrosorptive removal of sodium chloride, Carbon 47 (3) (2009) 775–781.

[34] Z. Peng, D. Zhang, L. Shi, T. Yan, High performance ordered mesoporous carbon/carbon nanotube composite electrodes for capacitive deionization, J. Mater. Chem. 22 (14) (2012) 6603–6612.

[35] H. Li, L. Zou, L. Pan, Z. Sun, Novel graphene-like electrodes for capacitive deionization, Environ. Sci. Technol. 44 (22) (2010) 8692–8697.

[36] S. Porada, L. Weinstein, R. Dash, A. Van Der Wal, M. Bryjak, Y. Gogotsi, P.M. Biesheuvel, Water desalination using capacitive deionization with microporous carbon electrodes, ACS Appl. Mater. Interfaces 4 (3) (2012) 1194–1199.

[37] L. Cseri, J. Baugh, A. Alabi, A. AlHajaj, L. Zou, R.A.W. Dryfe, P.M. Budd, G. Szekely, Graphene oxide-polybenzimidazolium nanocomposite anion exchange membranes for electrodialysis, J. Mater. Chem. A 6 (48) (2018) 24728–24739.

[38] L. Jheng, S.L. Hsu, B. Lin, Y. Hsu, Quaternized polybenzimidazoles with imidazolium cation moieties for anion exchange membrane fuel cells, J. Membr. Sci. 460 (2014) 160–170.

[39] K.Y. Law, Definitions for hydrophilicity, hydrophobicity, and superhydrophobicity: Getting the basics right, J. Phys. Chem. Lett. 5 (4) (2014) 686–688.

[40] G. Zhou, C. Xu, W. Cheng, Q. Zhang, W. Nie, Effects of oxygen element and oxygen-containing functional groups on surface wettability of coal dust with various metamorphic degrees based on XPS experiment, J. Anal. Methods Chem. 2015 (2015) 467242.

[41] S.E. Kentish, E. Kloester, G.W. Stevens, C.A. Scholes, L.F. Dumée, Electrodialysis in aqueous-organic mixtures, Sep. Purif. Rev. 44 (4) (2015) 269–282.

[42] K. Jo, Y. Baek, C. Lee, J. Yoon, Effect of hydrophilicity of activated carbon electrodes on desalination performance in membrane capacitive deionization, Appl. Sci. 9 (23) (2019) 5055.

[43] V.M. Palakkal, J.E. Rubio, Y.J. Lin, C.G. Arges, Low-resistant ion-exchange membranes for energy efficient membrane capacitive deionization, ACS Sustainable Chem. Eng. 6 (11) (2018) 13778–13786.

[44] L. Legrand, O. Schaetzle, R.C.F. De Kler, H.V.M. Hamelers, Solvent-free CO_2 capture using membrane capacitive deionization, Environ. Sci. Technol. 52 (16) (2018) 9478–9485.

[45] R. McNair, G. Szekely, R.A.W. Dryfe (2020), Ion-exchange materials for membrane capacitive deionization, ACS ES&T Water 1 (2) (2020) 217–223.